

π^-p Elastic Scattering at 2.26 GeV/c*

B. G. REYNOLDS, J. D. KIMEL, J. R. ALBRIGHT, R. H. BRADLEY, E. B. BRUCKER,
W. C. HARRISON, B. C. HARMS, J. E. LANNUTTI, W. H. SIMS, AND R. P. WIECKOWICZ

The Florida State University, Tallahassee, Florida 32306

(Received 20 May 1968)

The elastic scattering of negative pions on protons at 2.26 GeV/c has been studied using the Lawrence Radiation Laboratory 72-in. hydrogen-filled bubble chamber. The elastic scattering cross section is found to be 8.91 ± 0.24 mb. The forward diffraction peak is well fitted by an exponential in the square of the four-momentum transfer, and the slope is found to be 8.8 ± 0.1 GeV⁻². The differential cross section is parametrized in terms of three models: optical, strong-absorption, and two-slope. It is found that the two-slope model affords the best description of the data and also does very well in predicting the polarization data of other experiments. The best-fit parameters for all three models are given. In addition, the amplitudes associated with the best fits are given for the strong-absorption and the two-slope models.

I. INTRODUCTION

IN this paper we give the results of our analysis of 3941 elastic scattering events which occurred in a 2.26 ± 0.04 GeV/c π^- exposure of the Berkeley 72-in. hydrogen-filled bubble chamber. Preliminary results, which have been reported elsewhere,¹ encouraged us to undertake a more extensive study of elastic scattering at this energy. In particular, we were interested not only in reducing statistical uncertainties in fitted parameters by increasing the amount of data, but also in finding a parametrization which would also reproduce the polarization data,² available at our energy. We have fitted our differential cross section and the polarization data to the standard strong-absorption model of Dar *et al.*^{3,4} We also fitted our differential cross section to a two-slope model due to Kimel.⁵ This model not only improved the fit to the differential cross section but also successfully reproduced the polarization data and removed a number of difficulties inherent with the strong-absorption model.

II. EXPERIMENTAL METHODS

The elastic events of this experiment were selected from among 15 000 measured two-prong events by use of the Berkeley PANAL-PACKAGE programs. Our selection criteria required that an event have a χ^2 probability $\geq 1\%$ and that the positive track ionization be consistent with that expected of a proton. In addition, a fiducial volume was chosen to eliminate events at the beginning and end of the bubble chamber. As a result, our analysis was restricted to 3941 elastic scattering events.

* Work supported in part by the U. S. Atomic Energy Commission.

¹ B. G. Reynolds, J. R. Albright, E. B. Brucker, W. C. Harrison, B. C. Harms, J. D. Kimel, and J. E. Lannutti, *Phys. Letters* **24B**, 311 (1967).

² R. J. Esterling, R. E. Hill, N. E. Booth, S. Suwa, and A. Yokosawa, Enrico Fermi Institute for Nuclear Studies Report No. EFINS 66-29 (unpublished).

³ W. E. Frahn and R. H. Venter, *Ann. Phys. (N. Y.)* **24**, 243 (1963).

⁴ B. Kozlowsky and A. Dar, *Phys. Letters* **20**, 311 (1966); **20**, 314 (1966).

⁵ J. D. Kimel (to be published).

In order to be certain that we had a reasonable sample of elastic scattering events for our analysis, we made an extensive study of fitting ambiguities and experimental biases.

We were concerned with (a) contamination of our sample of elastic scattering events by nonelastic interactions; (b) determining the effect on the elastic scattering differential cross section due to the loss of elastic events in kinematic reconstruction and fitting; and (c) correcting for the experimental scanning bias against short, recoil protons.

A. Ambiguous Events

We studied the effects of nonelastic events on our elastic scattering sample by considering that it was occasionally possible for an inelastic event to fit the elastic hypothesis. When this happened, the event may or may not have had a greater probability for fitting the correct (inelastic) hypothesis. We also allowed for the possibility that an event with more than one neutral particle may have fitted the elastic hypothesis. In this latter situation, there is no correct hypothesis which could be determined by geometric reconstruction and fitting. In order to investigate these possibilities, we generated a sample of simulated events for each possible type of final-state hypothesis using the program FAKE.⁶ These simulated events were then processed through the PANAL-PACKAGE programs and the χ^2 probabilities for each hypothesis were examined. It was found that the simulated three-or-more-body final states showed no tendency to fit the elastic hypothesis. The simulated elastic events would, however, occasionally best fit the $\pi^-p\pi^0$ or $\pi^-\pi^+n$ final-state hypothesis. Furthermore, as expected, some of the simulated elastic scattering events would fit the elastic hypothesis but with a very low χ^2 probability ($< 1\%$). On this basis, we concluded that the elastic scattering data were free of contaminations due to nonelastic events. Thus the problem was reduced to a study of those elastic scattering events that were

⁶ G. R. Lynch, University of California Radiation Laboratory Report No. UCRL-10335, 1962 (unpublished).

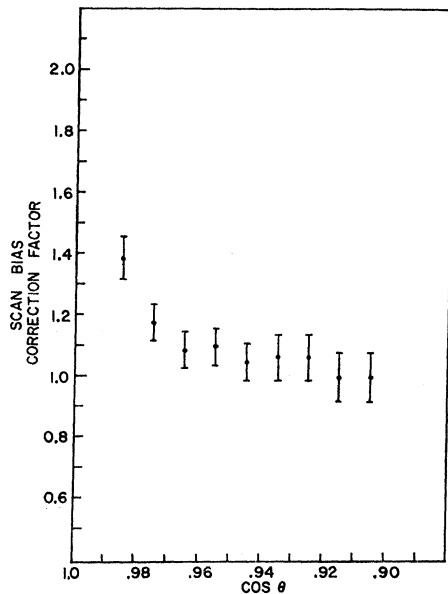


FIG. 1. The scan bias correction factor used to multiply the observed number of events in each $\cos\theta$ histogram interval.

lost from our sample in the fitting procedure by erroneously best-fitting a nonelastic hypothesis.

The ambiguities between the elastic scattering and $\pi^- \pi^+ n$ interpretations were easily resolved by the ionization requirement. The remaining events, all of which were ambiguous between the elastic scattering and $\pi^- p \pi^0$ hypothesis, were assigned to the elastic scattering category on the basis of the information obtained from the analysis of the simulated events. This problem has been studied by other physicists, who seem to have arrived at a similar conclusion.⁷ Thus our acceptance criteria for elastic scattering events may be stated as a χ^2 probability for the elastic hypothesis $> 1\%$ regardless of the χ^2 probability for any other hypothesis.

B. Events Lost in Reconstruction and Fitting

The simulated elastic scattering events were also used to study the type of events which were completely rejected by PACKAGE as (a) having no fit to any hypothesis or (b) simply failing to fit the elastic hypothesis. The first category was found to give an isotropic distribution for $\cos\theta$, the cosine of the π^- c.m. scattering angle. A small number of the simulated elastic scattering events (less than 1%) failed to fit the elastic hypothesis but did have a fit to an inelastic hypothesis. The distribution of these events was slightly asymmetric in favor of the region of $\cos\theta < 0$. This loss would result in a slight bias against the large-angle region of the elastic scattering differential cross section. However, since the number of large-angle scattering events is small, this loss would amount to only a 0.1% effect on the cross section in the

region of $\cos\theta < 0$ and can be neglected. We conclude that we have, within the statistical accuracy of this experiment, made a reasonably unbiased determination of the large-angle structure of the elastic scattering differential cross section at this energy.

C. Corrections for Scanning Bias

In the region of small scattering angle for the pion, corrections were made for scanning bias against short recoil protons. A correction factor was calculated for each histogram interval of the elastic scattering differential cross section by requiring an isotropic distribution for the angle ϕ , between the normal to the bottom of the bubble chamber and the normal to the plane of the

TABLE I. The $\pi^- p$ elastic differential cross section. Errors represent statistical uncertainties only.

$\cos\theta$	$d\sigma/d\Omega$ (mb/sr)	Error (mb/sr)
0.98	14.407	0.324
0.94	7.819	0.239
0.90	4.346	0.179
0.86	2.410	0.132
0.82	1.303	0.097
0.78	0.561	0.064
0.74	0.415	0.055
0.70	0.240	0.042
0.66	0.131	0.031
0.62	0.058	0.021
0.58	0.095	0.026
0.54	0.066	0.022
0.50	0.146	0.033
0.46	0.116	0.029
0.42	0.175	0.036
0.38	0.182	0.036
0.34	0.218	0.040
0.30	0.189	0.037
0.26	0.233	0.041
0.22	0.298	0.047
0.18	0.269	0.044
0.14	0.197	0.038
0.10	0.240	0.042
0.06	0.153	0.033
0.02	0.124	0.030
-0.02	0.102	0.027
-0.06	0.095	0.026
-0.10	0.138	0.032
-0.14	0.051	0.019
-0.18	0.044	0.018
-0.22	0.044	0.018
-0.26	0.044	0.018
-0.30	0.029	0.015
-0.34	0.015	0.010
-0.38	0.022	0.013
-0.42	0.015	0.010
-0.46	0.015	0.010
-0.50	0.022	0.013
-0.54	0.029	0.015
-0.58	0.015	0.010
-0.62	0.022	0.013
-0.66	0.007	0.007
-0.70	0.007	0.007
-0.74	0.007	0.007
-0.78	0.029	0.015
-0.82	0.036	0.016
-0.86	0.080	0.024
-0.90	0.080	0.024
-0.94	0.102	0.027
-0.98	0.051	0.019

⁷ D. D. Allen, G. P. Fisher, G. Godden, J. B. Kopelman, L. Marshall, and R. Sears, *Phys. Letters* **21**, 468 (1966).

scattering. Thus we required that the azimuthal angle of the scattered π^- be distributed isotropically. This requirement was not met in the region $0.98 \geq \cos\theta \geq 0.92$. For $\cos\theta < 0.92$ the distribution in ϕ was found to be isotropic and no correction for this scanning bias was necessary. Figure 1 shows the correction factor as a function of $\cos\theta$.

A different correction technique was necessary for the region of $\cos\theta > 0.98$ since event loss due to scanning bias was found to exist for all values of the angle ϕ . We estimated the correct number of events in this region by making a straight-line extrapolation through the nearby data points of the differential cross section.

The total number of events observed in this experiment was corrected for scanning bias and scanning efficiency to give the total number of events for cross-section determinations. This was normalized to the total π^- -proton cross section as determined by Diddens *et al.*⁸ This procedure gave an elastic scattering cross section of

$$\sigma_{el} = 8.91 \pm 0.24 \text{ mb.}$$

The elastic scattering differential cross section plotted as a function of $\cos\theta$, the cosine of the π^- scattering angle, is shown in Fig. 2. The data are also tabulated in Table I along with the statistical uncertainties in each

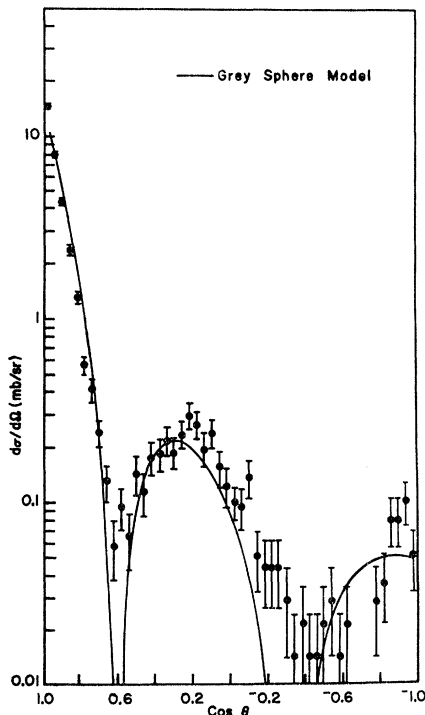


FIG. 2. The elastic scattering differential cross section as a function of $\cos\theta$, the cosine of the π^- c.m. scattering angle. The error bars on these data points represent statistical uncertainties. The solid curve represents a gray-sphere optical-model fit to the data.

⁸ A. N. Diddens, E. W. Jenkins, T. F. Kycia, and K. F. Riley, Phys. Rev. Letters **10**, 262 (1963).

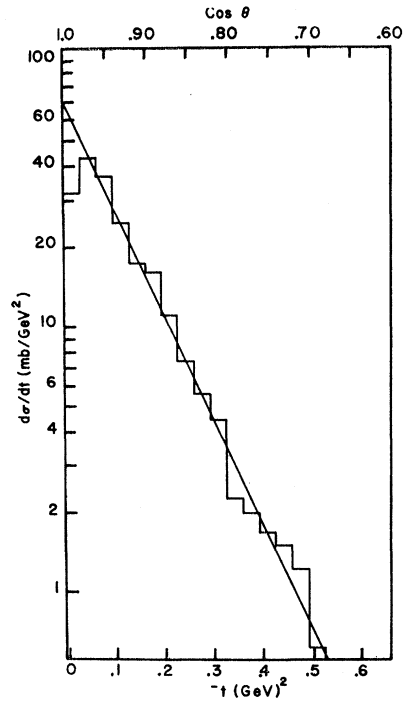


FIG. 3. Dependence of the elastic scattering differential cross section on the squared four-momentum transfer to the proton. The solid line results from a least-squares fit to the data and has a slope of 8.8 GeV^{-2} .

point. These uncertainties do not include an over-all uncertainty due to the normalization of $\pm 3\%$.

III. ELASTIC SCATTERING DIFFERENTIAL CROSS SECTION

The experimental value of the differential cross section at $\cos\theta = 1.0$, as determined by the straight-line extrapolation method described above, is $19.50_{-0.66}^{+0.68} \text{ mb/sr}$. These uncertainties include a 3% uncertainty in normalization. This value can be compared with the optical-theorem prediction for the square of the imaginary part of the forward-scattering amplitude. The optical-theorem value for this experiment is $17.84 \pm 0.70 \text{ mb/sr}$. The two values disagree by more than one standard deviation. Using dispersion-relation calculations for the real part of the forward-scattering amplitude at this energy⁹ and the optical-theorem value for the imaginary part of the forward amplitude we can calculate the total forward-scattering amplitude. We obtain

$$\begin{aligned} (d\sigma/d\Omega)(0^\circ) &= |\text{Im}f(0^\circ)|^2 + |\text{Re}f(0^\circ)|^2 = 17.84 \text{ mb/sr} \\ &\quad + 0.40 \text{ mb/sr} = 18.24 \pm 0.73 \text{ mb/sr.} \end{aligned}$$

This latter value is consistent with our experimental

⁹ G. Höhler, G. Ebel, and J. Giesecke, Z. Physik **180**, 430 (1964).

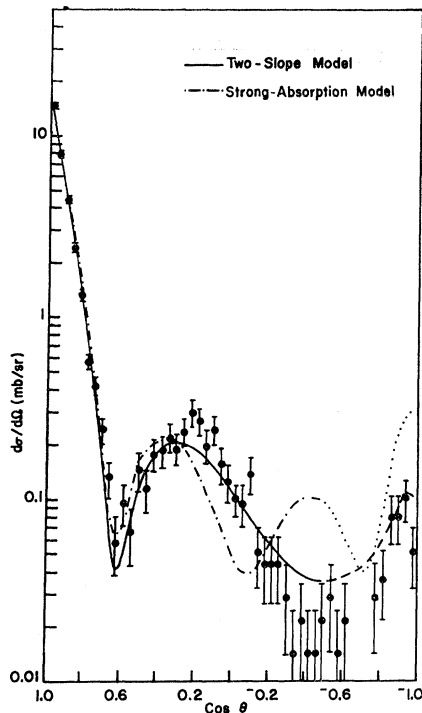


FIG. 4. The elastic scattering differential cross section. The dot-dashed curve represents the SAM fit to the data. The dotted curve is the extension of this model beyond the fitted region. The solid curve is the TSM fit to the data. The dashed curve is the extension of this model beyond the fitted region.

value. In addition, these results are consistent with other experiments in this energy region.¹⁰⁻¹²

The discussion of the differential cross section may be divided into four regions: (a) the forward diffraction peak, (b) the second maximum at $\cos\theta \approx 0.3$, (c) the intermediate $\cos\theta$ region, and (d) the backward region near $\cos\theta = -1.0$.

The differential cross section in the region of the forward diffraction peak is well fitted by an exponential in $-t$, the square of the four-momentum transfer to the proton, out to $\cos\theta = 0.60$. We have fitted the $-t$ interval corresponding to $0.96 \geq \cos\theta \geq 0.64$ to an expression of the form $d\sigma/dt = Ae^{Bt}$. The best fit obtained gave $A = 71.44_{-1.54}^{+1.44}$ mb/GeV² and $B = 8.8 \pm 0.1$ GeV⁻² and is displayed with the data in Fig. 3. When our value of B is compared with values found in other experiments in this energy region,¹⁰⁻¹³ it is seen that our slope does not agree, within one standard deviation, with all the experiments in the lab momentum interval

1.5–4.0 GeV/ c . It has been pointed out by Jacobs¹⁰ that there seems to be a variation in the slope of the diffraction peak in this region. Such an effect may be due to the π -nucleon resonances in this region.

The second maximum occurs at $\cos\theta \approx 0.3$ or $-t \approx 1.2$ GeV² in our data. This phenomenon seems to be present, at this value of $-t$, in all experiments in the several-GeV region up to lab momenta of about 4.0 GeV/ c .¹⁴ The energy dependence of this peak seems to show up as a changing of its shape and size rather than a shift in its central position.¹⁰⁻¹⁴

The intermediate $\cos\theta$ region from about -0.1 to -0.8 , while of interest in the study of resonance effects,¹⁰ is statistically the least significant portion of our data. Although the data clearly support the existence of a second minimum, the precise location of the minimum in this region is made uncertain by the statistical fluctuations.

The backward region is characterized by a significant rise in the differential cross section for $\cos\theta \leq -0.8$. However, there is a slight indication that this backward increase falls again before reaching $\cos\theta = -1.0$. This would be consistent with the results of 180° back-scattering counter experiments of Kormanyos *et al.*¹⁵

IV. ANALYSIS OF DIFFERENTIAL CROSS SECTION

A. Optical Model

We first fit the differential cross section from $\cos\theta = 0.96$ to -0.10 with a simple two-parameter optical model.¹⁶ This model treats the target nucleon as a gray sphere of radius R and transparency ϵ . The differential cross-section parametrization of this model is

$$\frac{d\sigma}{d\Omega} = (1 - \epsilon)^2 R^2 \left[\frac{J_1(2kR \sin \frac{1}{2}\theta)}{2 \sin \frac{1}{2}\theta} \right]^2.$$

The best least-squares fit to the data was obtained for $R = 0.93 \pm 0.01$ F and $\epsilon = 0.45 \pm 0.01$. The differential cross section corresponding to these values of the model parameters is given by the solid curve in Fig. 2.

B. Strong-Absorption Model

The strong-absorption model (SAM) has been applied recently with some success to the description of meson-baryon elastic scattering⁴ as well as to photoproduction of vector mesons at high energies.¹⁷ In this model the

¹⁴ M. N. Focacci and G. Giacomelli, CERN Report No. 18, 1966 (unpublished).

¹⁵ S. W. Kormanyos, A. D. Krisch, J. R. O'Fallon, K. Ruddick, and L. G. Ratner, Phys. Rev. **164**, 1661 (1967).

¹⁶ R. J. Glauber, in *Lectures in Theoretical Physics at the University of Colorado*, edited by E. Brittin and L. G. Dunham (Interscience Publishers, Inc., New York, 1959), Vol. I.

¹⁷ Y. Eisenberg, E. E. Ronat, A. Brandstetter, A. Levy, and E. Gotsman, Phys. Letters **22**, 217 (1966); Brown-Harvard-MIT-Padova-Weizmann Institute Bubble Chamber Group, Phys. Rev. **155**, 1468 (1967).

¹⁰ L. D. Jacobs, University of California Radiation Laboratory Report No. UCRL-16877, 1966 (unpublished).

¹¹ W. Busza, D. G. Davis, B. G. Duff, F. F. Heymann, P. V. March, C. C. Nimmon, D. T. Walton, E. H. Bellamy, T. F. Buckley, A. Stefanini, J. A. Strong, and R. N. F. Walker, Nuovo Cimento **52**, 331 (1967).

¹² D. E. Damouth, L. W. Jones, and M. L. Perl, Phys. Rev. Letters **11**, 287 (1963).

¹³ C. T. Coffin, N. Dikmen, L. Ettlinger, D. Meyer, A. Saulys, K. Terwilliger, and D. Williams, Phys. Rev. **159**, 1169 (1967).

π^-p elastic scattering process is parametrized directly in terms of the complex S -matrix elements η_l^\pm (for which $J=l\pm\frac{1}{2}$) occurring in the non-spin-flip and spin-flip amplitudes,

$$f_1(\theta) = \frac{i}{2k} \sum_{l=0}^{\infty} [(l+1)(1-\eta_l^+) + l(1-\eta_l^-)] P_l(\cos\theta) \quad (1)$$

and

$$g_1(\theta) = \frac{1}{2k} \sum_{l=1}^{\infty} [\eta_l^+ - \eta_l^-] P_l^1(\cos\theta). \quad (2)$$

Conventionally, η_l^\pm is approximated by

$$\text{Re}\eta_l^\pm = g(l) + \epsilon[1 - g(l)] \quad (3)$$

and

$$\text{Im}\eta_l^\pm = \mu dg(l)/dl \quad (4)$$

in the non-spin-flip amplitude where spin-dependent forces are neglected. In the spin-flip amplitude, however, these forces are taken crudely into account by the assumption⁴

$$\eta_l^+ - \eta_l^- \simeq i \text{Im}(\eta_l^+ - \eta_l^-) = i\nu d^2g(l)/dl^2, \quad (5)$$

where l is the orbital angular momentum parameter and $g(l)$ is of the Woods-Saxon form, i.e., $g(l) = \{1 + \exp[(L_0 - l)/\Delta]\}^{-1}$. Thus the SAM parametrizes the scattering amplitudes in terms of five parameters: L_0 , an orbital angular momentum parameter for which $g(l) = \frac{1}{2}$; Δ , the width parameter of $g(l)$; μ , the strength of the imaginary part of η_l^\pm ; ϵ , the transparency for low l ; and ν , which is a measure of the spin-orbit coupling.

Since our experimental c.m. energy, 2.27 GeV, lies in a region where s -channel resonances should contribute significantly to the elastic scattering amplitudes, we have added coherently to the SAM background amplitudes $f_1(\theta)$ and $g_1(\theta)$, the 11 better-known resonance amplitudes.¹⁸ The parameters used for the resonances are given in Table II. The resulting total amplitudes

TABLE II. Parameters for the $Y=+1$ fermion resonance states (Ref. 18).

Resonance mass (MeV)	Spin-parity (J^P)	Width Γ (MeV)	Elasticity (X_l)
$N_\alpha(1683)$	$\frac{3}{2}^+$	105	1.04
$\Delta_s(1236)$	$\frac{3}{2}^+$	120	1.0
$\Delta_s(1929)$	$\frac{3}{2}^+$	170	0.49
$\Delta_s(2452)$	$\frac{1}{2}^+$	275	0.117
$\Delta_s(2850)$	$\frac{1}{2}^+$	400	0.028
$\Delta_s(3230)$	$19/2^+$	440	0.003
$N_\gamma(1518)$	$\frac{3}{2}^-$	125	0.77
$N_\gamma(2216)$	$\frac{7}{2}^-$	240	0.25
$N_\gamma(2633)$	$\frac{1}{2}^-$	425	0.076
$N_\gamma(3030)$	$\frac{1}{2}^-$	400	0.011
$N_\gamma(3350)$	$19/2^-$	100	0.003

¹⁸ V. Barger and M. Olsson, Phys. Rev. **151**, 1123 (1966).

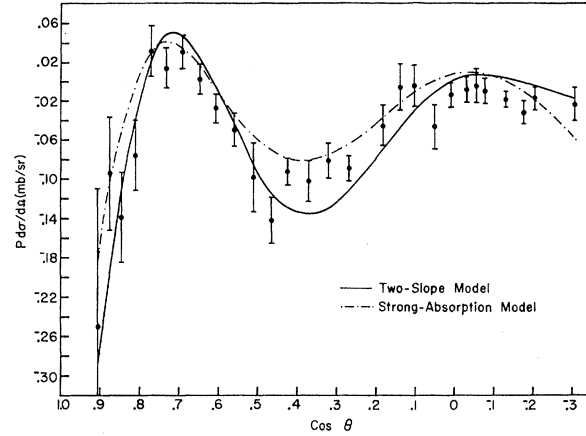


FIG. 5. Plot of $P(\theta)(d\sigma/d\Omega)(\theta)$. Dot-dashed curve: SAM fit to the data; solid curve: TSM prediction. The experimental data points (with error bars) are taken from Ref. 2.

$f_{1,\text{tot}}(\theta)$ and $g_{1,\text{tot}}(\theta)$ can be written

$$\begin{aligned} f_{1,\text{tot}}(\theta) &= f_1(\theta) + f_{\text{res}}(\theta), \\ g_{1,\text{tot}}(\theta) &= g_1(\theta) + g_{\text{res}}(\theta), \end{aligned} \quad (6)$$

where

$$\begin{aligned} f_{\text{res}}(\theta) &= \frac{1}{k} \left[\frac{1}{3} \sum_{\Delta_s} X_{3/2}(J+\frac{1}{2}) P_l(\cos\theta) / (E-i) \right. \\ &\quad \left. + \frac{2}{3} \sum_{N_\alpha, N_\gamma} X_{1/2}(J+\frac{1}{2}) P_l(\cos\theta) / (E-i) \right], \end{aligned} \quad (7)$$

and

$$\begin{aligned} g_{\text{res}}(\theta) &= \frac{i}{k} \left[\frac{1}{3} \sum_{\Delta_s} X_{3/2} P_l^1(\cos\theta) / (E-i) \right. \\ &\quad \left. - \frac{2}{3} \sum_{N_\alpha, N_\gamma} X_{1/2} P_l^1(\cos\theta) / (E-i) \right]. \end{aligned} \quad (8)$$

The sums of (7) and (8) refer to the resonant states listed in Table II; X_l represents the elasticity parameter of the resonance; J and l are the total and orbital angular momentum parameters; and $E = (M^2 - s)/M\Gamma$, where s , M , and Γ are the square of the c.m. energy, the resonance mass, and the full width of the resonance, respectively.

Since the five-parameter strong-absorption model describes the polarization

$$P(\theta)(d\sigma/d\Omega)(\theta) = 2 \text{Re}[f_{1,\text{tot}}(\theta)g_{1,\text{tot}}^*(\theta)] \quad (9)$$

as well as the differential cross section

$$(d\sigma/d\Omega)(\theta) = |f_{1,\text{tot}}(\theta)|^2 + |g_{1,\text{tot}}(\theta)|^2, \quad (10)$$

we have combined the polarization measurements of Suwa *et al.*² at 2.27 GeV/ c pion laboratory momentum with our experimental differential cross section and have fitted this model, using the method of least squares, to the two sets of data simultaneously over the range $1.0 \geq \cos\theta \geq -0.5$. The backward-direction limit of $\cos\theta = -0.5$ was chosen to exclude the region of the data in

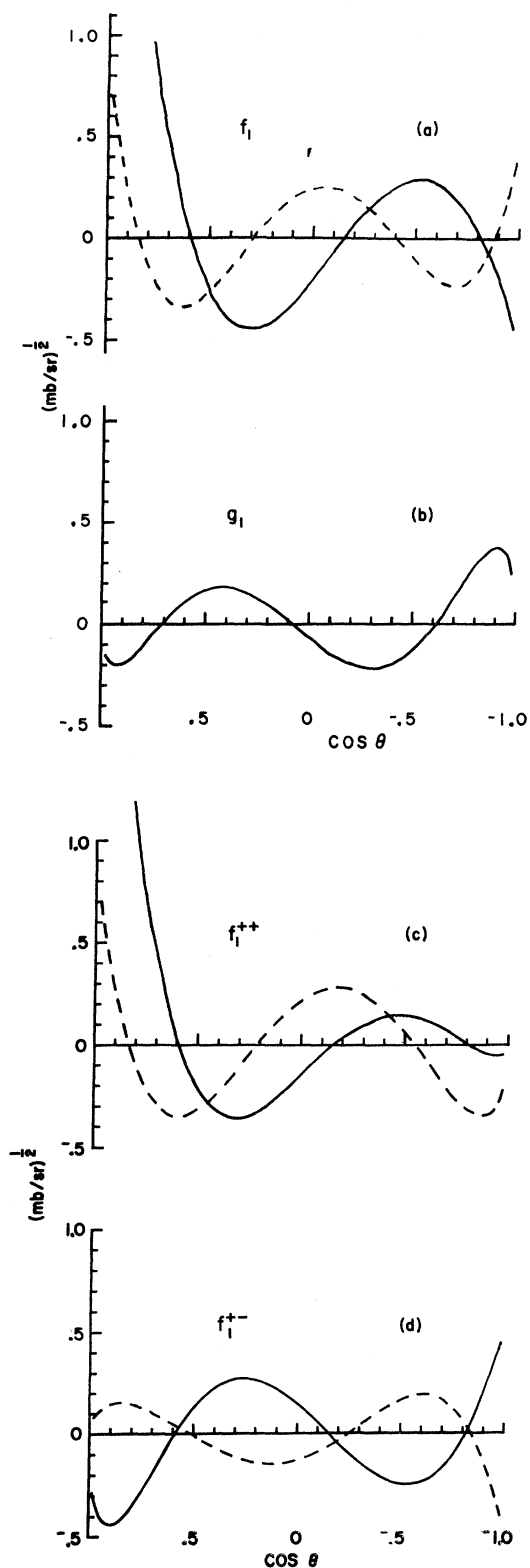


FIG. 6. The SAM background amplitudes: (a) spin-non-flip, (b) spin-flip, (c) helicity-non-flip, and (d) helicity-flip. Solid (dashed) curves correspond to the imaginary (real) parts of the amplitudes.

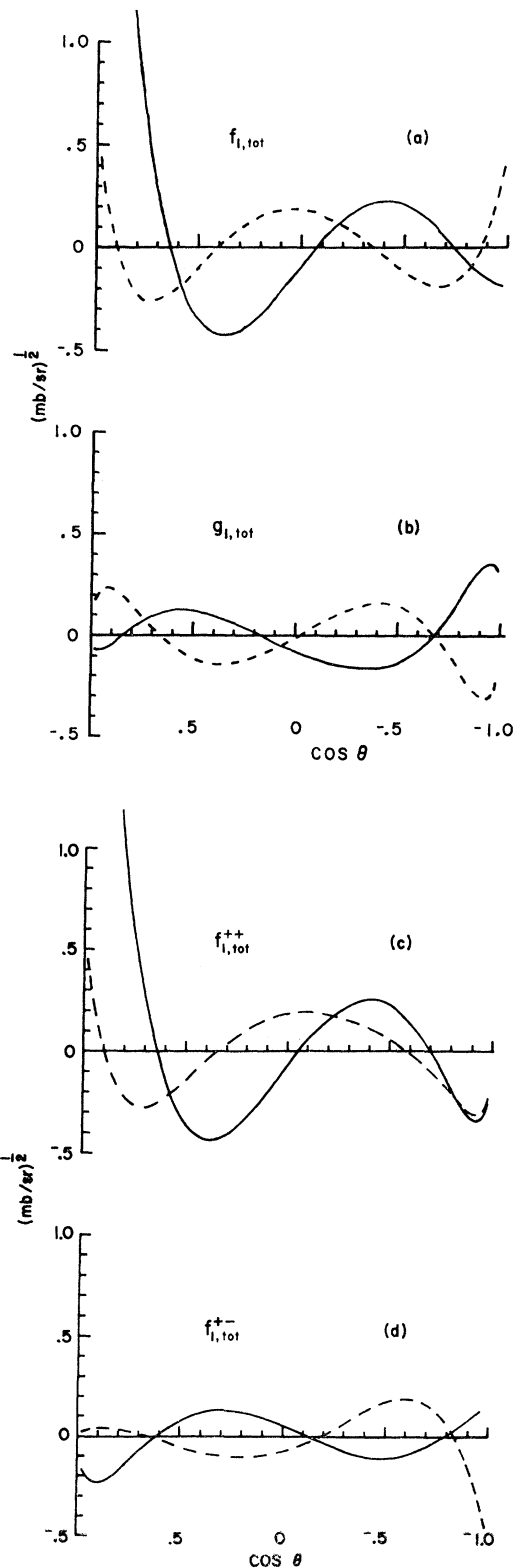


FIG. 7. Total (SAM background plus resonance) amplitudes: (a) spin-non-flip, (b) spin-flip, (c) helicity-non-flip, and (d) helicity-flip. Solid (dashed) curves correspond to the imaginary (real) parts of the amplitudes.

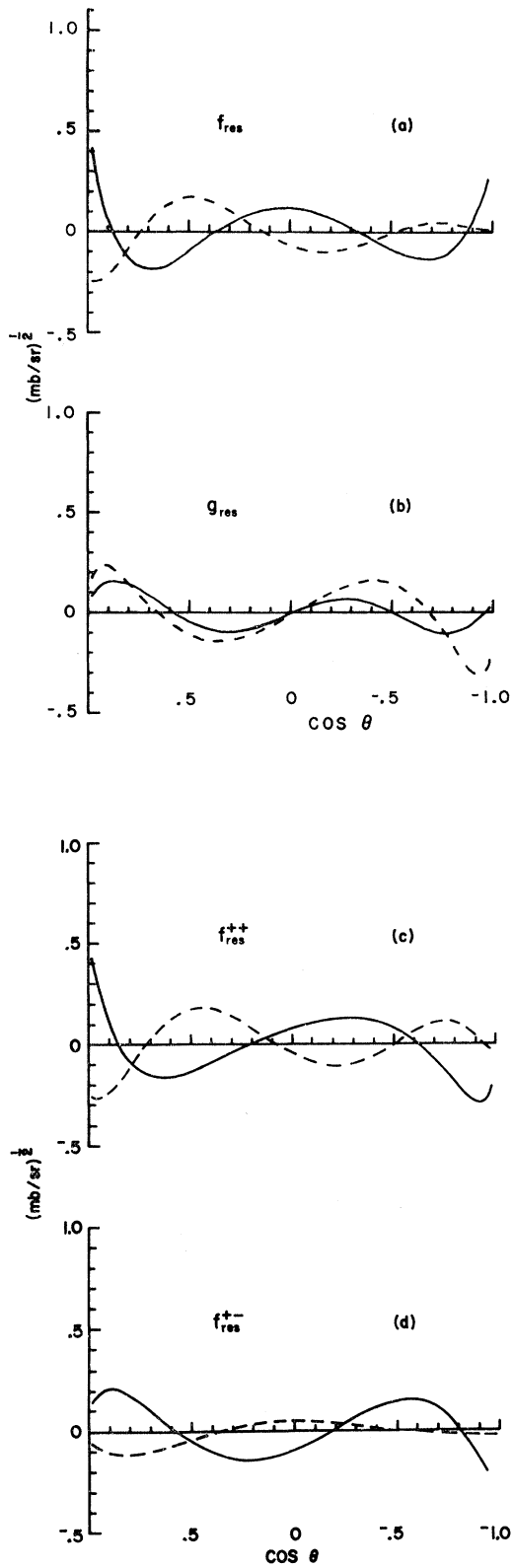


FIG. 8. The resonance amplitudes: (a) spin-nonflip, (b) spin-flip, (c) helicity-non-flip, (d) helicity-flip. Solid (dashed) curves correspond to the imaginary (real) parts of the amplitudes.

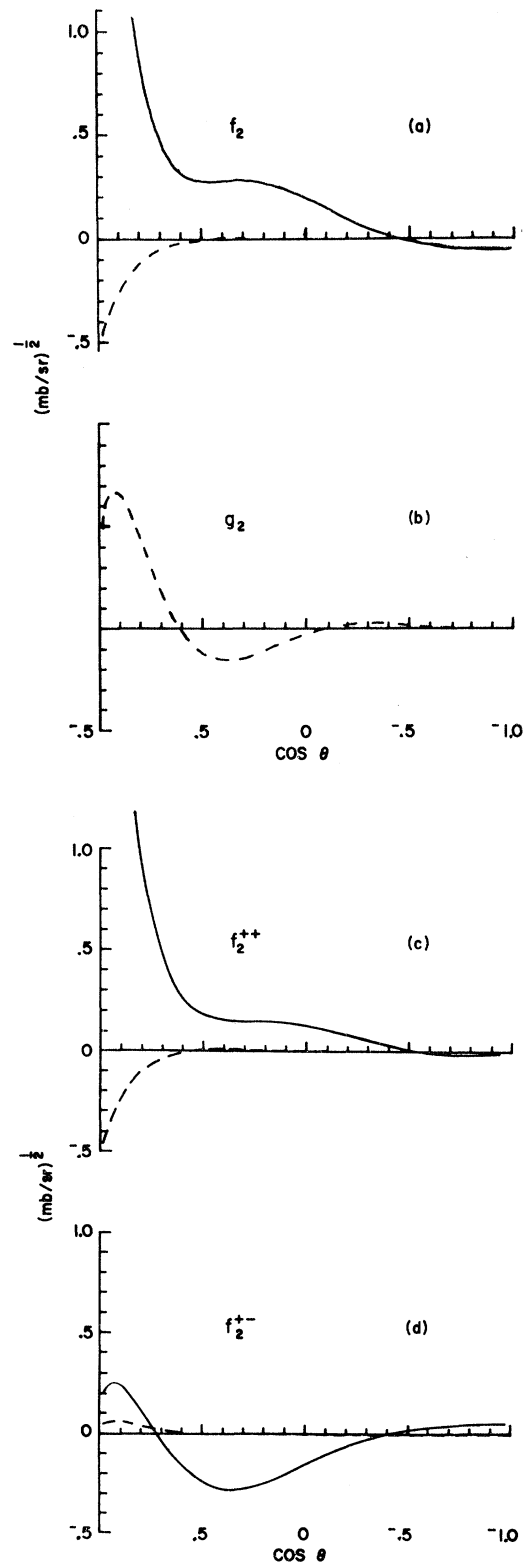


FIG. 9. The TSM background amplitudes: (a) spin-nonflip, (b) spin-flip, (c) helicity-non-flip, and (d) helicity-flip. Solid (dashed) curves correspond to the imaginary (real) parts of the amplitudes.

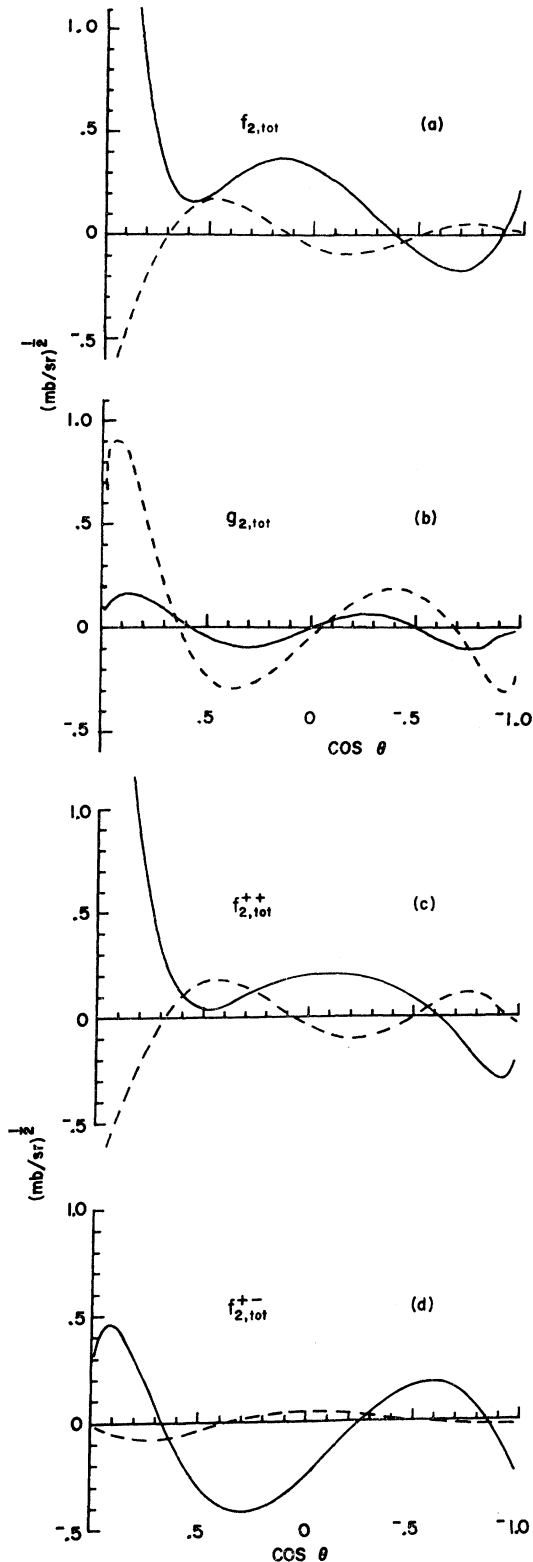


FIG. 10. Total (TSM background plus resonance) amplitudes: (a) spin-non-flip, (b) spin-flip, (c) helicity-non-flip, and (d) helicity-flip. Solid (dashed) curves correspond to the imaginary (real) parts of the amplitudes.

which baryon exchange may be expected to play a significant role.

The best fit ($\chi^2=250$ with 65 data points) occurred when

$$\begin{aligned} R &= 0.871 \pm 0.001 F, & d &= 0.039 \pm 0.001 F, \\ \mu/\Delta &= 2.3 \pm 0.2, & \epsilon &= 0.45 \pm 0.01, \\ \nu &= 0.148 \pm 0.005, \end{aligned}$$

where, for convenience, we have introduced a "radius" R and "diffuseness" d , which are related to L_0 and Δ by the definitions $kR = L_0 + \frac{1}{2}$ and $kd = \Delta$. The uncertainties given are entirely statistical. The differential cross section and polarization corresponding to these parameters are shown by the dot-dashed curves in Figs. 4 and 5, respectively. The SAM background amplitudes and the total amplitudes are shown in Figs. 6 and 7. It is useful to display the results also in the helicity representation. The helicity amplitudes are linear combinations of the non-spin-flip amplitude $f(\theta)$ and the spin-flip amplitude $g(\theta)$

$$\begin{aligned} f^{++}(\theta) &= f(\theta) \cos \frac{1}{2}\theta + ig(\theta) \sin \frac{1}{2}\theta, \\ f^{+-}(\theta) &= ig(\theta) \cos \frac{1}{2}\theta - f(\theta) \sin \frac{1}{2}\theta, \end{aligned} \quad (11)$$

where $f^{++}(\theta)$ and $f^{+-}(\theta)$ are the helicity-non-flip and helicity-flip amplitudes, respectively.¹⁹ The background and total amplitudes in this representation are also shown in Figs. 6 and 7. For comparison the resonance amplitudes alone are plotted in both representations in Fig. 8.

The following points should be noted concerning the SAM parametrization of the data:

(a) In the forward direction the SAM predicts a "bowed" diffraction peak of the form

$$d\sigma/d\Omega \propto \{J_1[(L_0 + \frac{1}{2})\theta]/\theta\}^2$$

rather than $d\sigma/d\Omega \propto e^{At}$, which would be more consistent with the experimental data.

(b) The dip in the differential cross section at $\cos\theta \simeq 0.6$ is attributed to a zero in $\text{Im}f_{1,tot}(\theta)$.

(c) The secondary maximum in the differential cross section is not well reproduced and again is attributed mainly to $\text{Im}f_{1,tot}(\theta)$. Since $\text{Im}f_1(\theta)$ is negative in the region of the secondary maximum, the resonance amplitude $f_{res}(\theta)$, which is dominated by the G -wave $N(2190)$ at our energy, tends to cancel the SAM background amplitude in this region, with the result that the secondary maximum is better reproduced with SAM background amplitudes alone.¹

(d) The SAM background spin-flip amplitude $\text{Im}g_1(\theta)$ is important in fitting the polarization but contributes little to the differential cross section in the region of the secondary maximum.

(e) In order for this model to fit the polarization data with resonances present, $\text{Re}f_{1,tot}(0)$ must be positive,

¹⁹ We follow here M. Jacob and G. C. Wick, *Ann. Phys. (N. Y.)* **7**, 404 (1959).

but this is in contradiction to the results of forward dispersion relations.⁹

C. Two-Slope Model

In view of the deficiencies in the strong-absorption model, we have also fitted the data using the two-slope model (TSM) suggested by Kimel,⁵ in which one parametrizes meson-baryon elastic scattering essentially in terms of two absorptive Gaussian diffraction regions and an absorptive "surface" region. Thus the TSM S -matrix elements are written

$$\text{Re}\eta_{l^\pm} = 1 - \alpha g_1(l) - (1 - \alpha)g_2(l) - \gamma_\pm S_1(l), \quad (12)$$

where $g_1(l) = \exp(-l^2/L_1^2)$ and $g_2(l) = \exp(-l^2/L_2^2)$ correspond to the contributions to the elastic transition amplitude from the two Gaussian absorptive diffraction regions. An absorptive surface term $S_1(l)$ was, for convenience, taken to be of the form $S_1(l) = \exp[-(l-L_1)^2/\Delta_1^2]$. In order to satisfy forward dispersion relations, the model assumes an imaginary term which contributes to the real part of the non-spin-flip amplitude in the forward direction;

$$\text{Im}\eta_{l^\pm} = Kg_1(l).$$

The resulting background amplitudes $f_2(\theta)$ and $g_2(\theta)$ depend on six independent parameters: R_1 (with $kR_1 \equiv L_1 + \frac{1}{2}$) and R_2 (with $kR_2 \equiv L_2 + \frac{1}{2}$), the "radii" of the outer and inner diffraction regions; α , the outer absorption parameter; d_1 (with $kd_1 \equiv \Delta_1$), the width of the surface absorptive region; and γ_\pm , the strengths of the surface absorption for $J = l \pm \frac{1}{2}$. [It is clear from (12) that $\text{Re}\eta_{0^\pm}$ is completely absorbed in this model.²⁰] The parameter K was fixed by forward dispersion relations as discussed below.

As in Sec. IV B for the SAM, the TSM background amplitudes $f_2(\theta)$ and $g_2(\theta)$ were added coherently to the s -channel resonance amplitudes to form the total amplitudes $f_{2,\text{tot}}(\theta)$ and $g_{2,\text{tot}}(\theta)$. The parameter K was fixed at $K = -0.1$ by the forward-dispersion-relation requirement that $\text{Re}f_{2,\text{tot}}(0)/\text{Im}f_{2,\text{tot}}(0) \simeq -0.2$.⁹ Since the other parameters of this model, unlike those of the strong-absorption model, could be determined by a fit to the differential cross-section data alone, we used the polarization data only as a consistency check and fitted the model to our experimental differential cross section alone over the range $1.0 \geq \cos\theta \geq -0.5$. The best-fit

parameters with statistical uncertainties are

$$\begin{aligned} R_1 &= 0.85 \pm 0.01 \text{ F}, & R_2 &= 0.42 \pm 0.01 \text{ F}, \\ \alpha &= 0.25 \pm 0.02, & d_1 &= 0.38 \pm 0.02 \text{ F}, \\ \gamma_+ &= 0.007 \pm 0.009, & \gamma_- &= 0.29 \pm 0.01, \end{aligned}$$

corresponding to a χ^2 of 39 with 37 data. The resulting fitted differential cross section and *predicted* polarization are shown by the solid curves in Figs. 4 and 5, respectively. The corresponding TSM background and total amplitudes are displayed in Figs. 9 and 10.

The main features of the TSM fit to the data may be summarized as follows:

(a) The amplitudes determined by fitting the differential cross section alone also do remarkably well in reproducing polarization data.

(b) In addition to being able to reproduce the exponential dependence in t of the differential cross section in the forward direction, it also simultaneously reproduces the secondary maximum.

(c) The dip in the angular distribution at $\cos\theta \simeq 0.6$ results from a zero in $\text{Im}f_{2,\text{tot}}^{+-}(\theta)$, which also produces a zero in the polarization at approximately the same position. $\text{Im}f_{2,\text{tot}}^{++}(\theta)$ falls monotonically in the region of the secondary maximum but remains positive. Here it is interesting to note the suggestion made by Frautschi on the basis of Regge theory that the dip in the differential cross section is due to the vanishing of the helicity-flip amplitude.²¹

(d) The structure in $d\sigma/d\Omega$ is primarily due to the imaginary parts of the helicity amplitudes, with the real parts playing a minor role.

ACKNOWLEDGMENTS

We wish to thank Professor Luis Alvarez of the University of California for permission to use the film for this experiment. We are also grateful to many members of the Alvarez group at the Lawrence Radiation Laboratory for assistance with our data-processing programs. We acknowledge the computer time and staff assistance made available to us by the FSU Computing Center. We also express our appreciation to the technical staff of Florida State University particle-physics group for much aid in all phases of this work. Finally, we wish to acknowledge conversations with Professor Marc Ross of the University of Michigan, and to thank Professor Norman E. Booth of the University of Chicago for sending us the polarization data.

²⁰ The contribution of $S_1(0)$ is negligible.

²¹ S. Frautschi, Phys. Rev. Letters 17, 722 (1966).